



HAL
open science

Disk Galaxies Are Self-similar: The Universality of the H I-to-Halo Mass Ratio for Isolated Disks

Marie Korsaga, Benoit Famaey, Jonathan Freundlich, Lorenzo Posti, Rodrigo Ibata, Christian Boily, Katarina Kraljic, D. Esparza-Arredondo, C. Ramos Almeida, Jean Koulidiati

► **To cite this version:**

Marie Korsaga, Benoit Famaey, Jonathan Freundlich, Lorenzo Posti, Rodrigo Ibata, et al.. Disk Galaxies Are Self-similar: The Universality of the H I-to-Halo Mass Ratio for Isolated Disks. The Astrophysical journal letters, 2023, 952, 10.3847/2041-8213/ace364 . insu-04178501

HAL Id: insu-04178501

<https://insu.hal.science/insu-04178501>

Submitted on 9 Nov 2023

HAL is a multi-disciplinary open access archive for the deposit and dissemination of scientific research documents, whether they are published or not. The documents may come from teaching and research institutions in France or abroad, or from public or private research centers.








L'archive ouverte pluridisciplinaire **HAL**, est destinée au dépôt et à la diffusion de documents scientifiques de niveau recherche, publiés ou non, émanant des établissements d'enseignement et de recherche français ou étrangers, des laboratoires publics ou privés.



Distributed under a Creative Commons Attribution 4.0 International License



Disk Galaxies Are Self-similar: The Universality of the H I-to-Halo Mass Ratio for Isolated Disks

Marie Korsaga^{1,2,4} , Benoit Famaey¹ , Jonathan Freundlich¹ , Lorenzo Posti¹ , Rodrigo Ibata¹ , Christian Boily¹,
Katarina Kraljic¹ , D. Esparza-Arredondo^{3,4}, C. Ramos Almeida^{3,4} , and Jean Kouldiaty²

¹ Université de Strasbourg, CNRS, Observatoire astronomique de Strasbourg, UMR 7550, F-67000 Strasbourg, France; marie.korsaga@astro.unistra.fr

² Laboratoire de Physique et de Chimie de l'Environnement, Université Joseph Ki-Zerbo, 03 BP 7021, Ouaga 03, Burkina Faso

³ Instituto de Astrofísica de Canarias, Calle Vía Láctea, s/n, E-38205, La Laguna, Tenerife, Spain

⁴ Departamento de Astrofísica, Universidad de La Laguna, E-38206, La Laguna, Tenerife, Spain

Received 2023 May 23; revised 2023 June 29; accepted 2023 July 2; published 2023 August 2

Abstract

Observed scaling relations in galaxies between baryons and dark matter global properties are key to shed light on the process of galaxy formation and on the nature of dark matter. Here, we study the scaling relation between the neutral hydrogen (H I) and dark matter mass in isolated rotationally supported disk galaxies at low redshift. We first show that state-of-the-art galaxy formation simulations predict that the H I-to-dark-halo mass ratio decreases with stellar mass for the most massive disk galaxies. We then infer dark matter halo masses from high-quality rotation curve data for isolated disk galaxies in the local Universe and report on the actual *universality* of the H I-to-dark halo mass ratio for these observed galaxies. This scaling relation holds for disks spanning a range of 4 orders of magnitude in stellar mass and 3 orders of magnitude in surface brightness. Accounting for the diversity of rotation curve shapes in our observational fits decreases the scatter of the H I-to-dark halo mass ratio while keeping it constant. This finding extends the previously reported discrepancy for the stellar-to-halo mass relation of massive disk galaxies within galaxy formation simulations to the realm of neutral atomic gas. Our result reveals that isolated galaxies with regularly rotating extended H I disks are surprisingly self-similar up to high masses, which hints at mass-independent self-regulation mechanisms that have yet to be fully understood.

Unified Astronomy Thesaurus concepts: [Spiral galaxies \(1560\)](#); [Dark matter distribution \(356\)](#); [Galaxy kinematics \(602\)](#); [Galaxy dynamics \(591\)](#); [Irregular galaxies \(864\)](#)

1. Introduction

The detailed study of the observed dynamics of galaxies and of the distribution of baryons within them led over the last decades to the establishment of important scaling relations linking the baryon content to the gravitational field of galaxies (see, e.g., Lelli 2022), which could improve our understanding of the galaxy formation process and possibly shed light on the nature of dark matter (DM). Most of these scaling relations either focus on the total amount of observable baryons in galaxies, such as in the baryonic Tully–Fisher relation (McGaugh et al. 2000; Lelli et al. 2019; Schombert et al. 2022), or on their stellar content, such as in the stellar-to-halo mass relation (SHMR; e.g., Moster et al. 2010; Behroozi et al. 2010; Moster et al. 2013; Posti et al. 2019), connecting the stellar mass of a galaxy to its DM halo mass.

The SHMR is particularly important as it indicates how much stellar mass has assembled out of the primeval amount of baryons expected in galaxies from the cosmic baryon fraction. It can also be compared to expectations from abundance matching, a technique that matches halos—from the theoretical halo mass function expected in the standard Λ CDM cosmological model—with observed galaxies, following a luminosity function with a very different shape. The SHMR expected from abundance matching cannot be represented by a simple power law and displays a turnover at high mass (e.g., Behroozi et al. 2010; Moster et al. 2010). This characteristic shape of the

SHMR is nowadays a clear constraint and output for most galaxy formation simulations (Schaye et al. 2015; Pillepich et al. 2018; Marasco et al. 2020). However, resolved galaxy rotation curves have revealed that the SHMR of nearby isolated disk galaxies is actually a simple power law with no turnover at high mass (Posti et al. 2019; Marasco et al. 2020; Posti & Fall 2021). Its linear shape on a logarithmic scale, together with other such scale-free relations (e.g., the baryonic Tully–Fisher relation and the mass–size relation), contribute to portraying isolated disks as a rescalable population of objects, implying self-regulating mechanisms that are yet to be fully understood.

On the other hand, less attention has been paid to the relationship between the cold gas and the DM content of disk galaxies, while it is known that cold gas plays a crucial role in the process of star formation. Here, we therefore focus on the less-explored neutral atomic hydrogen-to-halo mass relation (H I HMR). Similarly to the SHMR, various methods allow one to probe the H I HMR observationally, e.g., galaxy clustering (Guo et al. 2017; Padmanabhan & Refregier 2017; Obuljen et al. 2019; Calette et al. 2021), halo abundance matching (Popping et al. 2015; Padmanabhan & Kulkarni 2017; Chauhan et al. 2021), or H I spectral stacking (Guo et al. 2020). However, the main assumption of abundance matching, namely that there is a direct relation between the halo mass and a galaxy property, certainly does not hold for H I, which can be very sensitive to other factors, such as, e.g., its morphology. Recent studies, such as that of Dutta et al. (2022), have, for instance, attempted to derive the H I HMR for H I-selected galaxies only, also separating the sample into blue and red galaxies. Despite these various different methods and selections, a common finding of *all* these studies is that the relation



Original content from this work may be used under the terms of the [Creative Commons Attribution 4.0 licence](#). Any further distribution of this work must maintain attribution to the author(s) and the title of the work, journal citation and DOI.

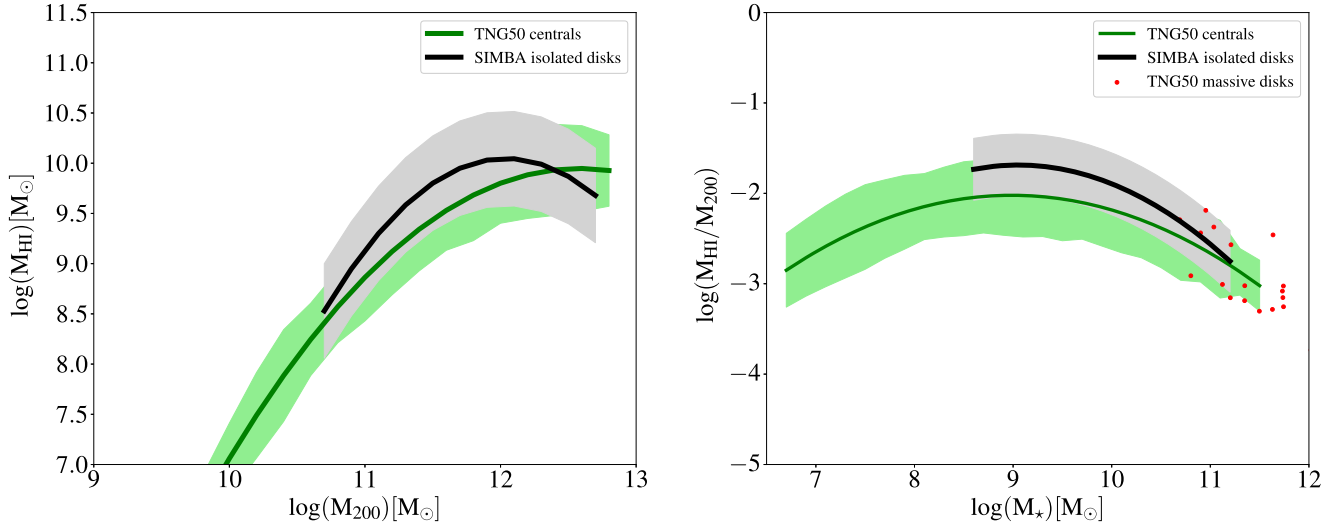


Figure 1. Left panel: H I mass vs. halo mass for $\sim 2.1 \times 10^4$ central galaxies (irrespective of morphology) in Illustris-TNG50 (green) and for 3180 isolated *disk* galaxies in SIMBA with $M_{200} \geq 10^9 M_\odot$ and $v/\sigma \geq 0.8$ (gray). The lines represent the median of the binned data, and the 1σ band around the median is represented by the green and gray bands, respectively. Right panel: H I mass to halo mass ratio vs. stellar mass. The 1σ band around the median is represented by the green and gray bands. Green: $\sim 2.1 \times 10^4$ centrals in TNG50. Red dots: simulated galaxies with $M_* > 5 \times 10^{10} M_\odot$ in TNG50 and with the fractional mass of stars with a stellar circularity $\epsilon > 0.7$ larger than 30%, hence disk galaxies in TNG50. Gray: 3180 isolated disk galaxies in SIMBA, with $M_{200} \geq 10^9 M_\odot$ and $v/\sigma \geq 0.8$.

between H I mass and halo mass at $z = 0$ is typically described by a double power law with a turnoff halo mass between 10^{11} and $10^{12} M_\odot$. This typically translates into a H I-to-halo mass ratio that varies with the galaxy halo mass or stellar mass with a peak and plateau around that characteristic mass and a decrease on both ends of the relation. However, all these determinations are slightly model dependent as they rely on an a priori knowledge of the halo mass function, and none of them are therefore *direct* determinations. Here, we will thus check whether this result holds when analyzing individual observed galaxy rotation curves of isolated disk galaxies in the local Universe and directly compare these results to the predictions of state-of-the-art galaxy formation simulations for disk galaxies.

2. The H I HMR in State-of-the-Art Simulations

2.1. Illustris-TNG50

We first investigate the H I HMR in the N -body/hydrodynamical simulations Illustris-TNG (Nelson et al. 2018; Pillepich et al. 2018; Nelson et al. 2019; Pillepich et al. 2019). We extracted from the highest-resolution realizations TNG50-1 (for which the mean baryon and DM particle mass resolutions are respectively $8.5 \times 10^4 M_\odot$ and $4.5 \times 10^5 M_\odot$), the central subhalos of stellar mass M_* , and DM halo mass M_{200} from the group catalog (which contains about 4.4 million subhalos) and cross-matched them with the supplementary HIH_2 catalog, computed in post-processing with the methods described in Diemer et al. (2018), to extract the corresponding H I mass ($\sim 3 \times 10^4$ subhalos). Selecting only halo masses $\geq 10^9 M_\odot$, we end up with 21,168 TNG50-1 central (and mostly isolated) galaxies at redshift $z = 0$ having H I mass available. Their distribution of H I versus stellar mass is displayed in Figure A1.

Figure 1 (left panel, green) is constructed using these 21168 TNG50-1 centrals, showing M_{HI} as a function of M_{200} . To check whether massive disk galaxies follow the same trend as the general population at high masses, we then concentrated on the 271 central galaxies with $M_{200} \geq 10^{12} M_\odot$: each of these

galaxies has H I mass associated to it in the supplementary HIH_2 catalog. We then selected disk galaxies among those, with a criterion based on having a stellar circularity parameter fraction $f(\epsilon > 0.7) > 0.3$ (Tacchella et al. 2019): this stellar circularity parameter for each stellar orbit, ϵ , is the ratio between the vertical component of the angular momentum and its value for a circular orbit. The right panel of Figure 1 shows in red dots the 18 galaxies with $M_* > 5 \times 10^{10} M_\odot$ and a circularity parameter fraction $f(\epsilon > 0.7) > 0.3$, which clearly shows that these galaxies do follow the break in M_{HI}/M_{200} at high stellar masses, suggesting that this predicted break is independent of the morphological type in the TNG50 simulation.

2.2. SIMBA

While it appears that massive disk galaxies in TNG50 display a decrease of the H I-to-dark halo mass ratio at the high-mass end, it should be noted that this conclusion is based on rather small number statistics, and most importantly that TNG50 does not resolve H I gas masses, which are treated in post-processing and therefore certainly subject to some non-negligible uncertainty. It is thus desirable to also investigate the H I HMR relation for disk galaxies in simulations that can compute H I masses self-consistently on the fly.

SIMBA⁵ (Davé et al. 2019) is a suite of cosmological hydrodynamical simulations run with a modified version of the gravity and hydrodynamics solver GIZMO (Hopkins 2015), based on the GADGET-3 gravity solver (Springel 2005). It tracks gas particles self-consistently, on the fly, via sub-grid prescriptions to account for molecular gas production, destruction, and approximates self-shielding that results in neutral gas. The H_2 is computed using the sub-grid prescription based on the local metallicity and gas column density following Krumholz & Gnedin (2011). The self-shielding that results in the total neutral gas is based on the prescription of Rahmati et al. (2013), with the ionizing flux strength attenuated

⁵ <http://simba.roe.ac.uk/>

depending on the gas density and assuming a spatially uniform ionizing background from Haardt & Madau (2012). Subtracting off the H_2 from the neutral gas then gives the H I contribution.

We analyze the SIMBA run following the evolution of 1024^3 DM and 1024^3 gas particles within a comoving volume of $(100 h^{-1} \text{ Mpc})^3$, but we checked that results are consistent if we concentrate on a higher-resolution $25 h^{-1} \text{ Mpc}$ volume with less statistics. To describe the morphology of galaxies, we use the kinematic ratio of their rotation- to dispersion-dominated velocity, v/σ . This quantity is computed from the 3D velocity distribution of stellar particles of each galaxy, the tangential velocity being computed in the plane perpendicular to the angular momentum of the stellar component of a galaxy. Note that this quantity is not directly comparable to observational measures of v/σ . We simply use it to separate rotation-dominated from dispersion-dominated systems. We select the 3180 central galaxies that have $M_{200} \geq 10^9 M_\odot$ and $v/\sigma \geq 0.8$ and that are isolated, which we consider as isolated disks. For the isolation criteria, we select those for which the number of galaxies in the halo is equal to one. Their distribution of H I versus stellar mass is displayed in Figure A1. It then appears clearly from Figure 1 (gray bands) that the conclusion reached from Illustris-TNG is confirmed with a much higher number of identified isolated disks and a self-consistent treatment of the gas in SIMBA.

3. Mass Modeling of Isolated Disks

After having analyzed the H I HMR of disk galaxies in two modern state-of-the-art galaxy formation simulations, we now turn to a direct comparison to data. As outlined in Section 1, most methods used to measure this relation are indirect and somewhat model dependent. A precise assessment of the H I HMR in disk galaxies can actually *only* be achieved through individual, detailed mass-modeling.

We start from a sample of 175 isolated nearby rotationally supported galaxies, namely 158 SPARC (Spitzer Photometry and Accurate Rotation Curves; Lelli et al. 2016) and 17 LITTLE THINGS (Local Irregulars That Trace Luminosity Extremes, The H I Nearby Galaxy Survey; Hunter et al. 2012; Oh et al. 2015; Iorio et al. 2017; Read et al. 2017) galaxies. To avoid systematic uncertainties related to inclination in nearly face-on systems, only SPARC galaxies with inclinations larger than 30° were kept in our analysis. All these galaxies were selected with observed extended H I disks and regular disklike kinematics. One has to keep in mind that all the observational results reported hereafter pertain to such *regularly rotating* disks, especially when comparing data to simulations. With this caveat in mind, we note that, in terms of M_{HI} versus M_* , the observed galaxies analyzed here are not outliers from the general population from the blind extragalactic H I survey ALFALFA (Maddox et al. 2015) and compare well with simulated ones.

To consider the contribution of the gas to the circular velocity for the LITTLE THINGS galaxies, we derived the expected circular velocity curve from the H I surface densities taken from Iorio et al. (2017) for which we applied a multiplicative factor of 1.33 to account for the presence of helium. Since these galaxies are very gas rich, the stellar mass-to-light ratios from their B -band photometry are less important to know precisely than for most SPARC galaxies. For the latter, $3.6 \mu\text{m}$ photometry allows to minimize the variations of the stellar mass-to-light ratios from stellar population synthesis

models (McGaugh & Schombert 2014; Meidt et al. 2014; Schombert et al. 2019).

To investigate the relation between neutral hydrogen and DM mass within the sample, we then produced mass models with two analytical DM profiles: (i) the standard Navarro–Frenk–White (NFW; Navarro et al. 1996) cuspy density profile, characterized by a dimensionless concentration parameter c and the halo mass (M_{200}), and (ii) the so-called Dekel–Zhao (DZ; Zhao 1996; Dekel et al. 2017; Freundlich et al. 2020) profile, characterized by a variable inner slope (s_1) defined as the absolute value of the logarithmic slope at 1% of the virial radius, a dimensionless concentration parameter c and the halo mass (M_{200}). We assume a Gaussian prior for the logarithm of the mass-to-light ratio of the stellar disk, centered on $M/L_{\text{disk}} = 0.6 M_\odot/L_\odot$ with a dispersion $\sigma = 0.2$ dex for SPARC data and centered on $1 M_\odot/L_\odot$ with $\sigma = 0.2$ dex for the B -band LITTLE THINGS data, which broadly encompasses the values expected from stellar population synthesis models (McGaugh & Schombert 2014; Meidt et al. 2014). For the halo concentration c , we assume a Gaussian prior that follows the c - M_{200} relation as estimated in Dutton & Macciò (2014) with a scatter of 0.11. For the DM halo mass M_{200} , we use a flat prior over a wide range of $0 \leq \log M_{200}/M_\odot \leq 20$. For galaxies with a spherical bulge component, we assume that $M/L_{\text{bulge}} = 1.4 \times M/L_{\text{disk}}$, as suggested by stellar population synthesis models Schombert & McGaugh (2014). For the additional free parameter s_1 of the DZ profile, we assume a flat prior in the range $0 \leq s_1 \leq 5$.

The parameters are then fitted using an affine-invariant Markov Chain Monte Carlo (MCMC) sampling with the Python implementation EMCEE (Foreman-Mackey et al. 2013). For each parameter, we take the median of the marginalized posterior as the best-fit value while lower and upper errors are taken at the 16th and 84th percentiles. For 25 galaxies, typically with $\log(M_{200}) < 9$, the fits are of very bad quality in both cases, and we left these galaxies out of our analysis, ending up with a sample of 150 galaxies for both profiles NFW and DZ.

The reduced χ^2 values for all NFW and DZ fits are given in Table B1. The median reduced χ^2 is 1.93 for NFW (with a large dispersion of 5.3, toward very bad fits) and 1.05 for DZ (with a dispersion of 2.8). An example is given in Figure B1. In the following, we concentrate on the DZ profile, which gives significantly better fits, taking into account the full diversity of rotation curve shapes. The median stellar mass-to-light ratio for the DZ fits of the SPARC galaxies is $M/L_{\text{disk}} = 0.53 M_\odot/L_\odot$. The median is closer to the prior for NFW fits (0.57), but it is in this case boosted by some high values from poor NFW fits.

4. Results

While we concentrate hereafter on the results obtained from the DZ fits, most of the scaling relations reported hereafter are unaltered when using NFW profiles, with one exception (the independence on surface brightness), but the *scatter* around the scaling relations typically increases when using NFW fits, meaning that better individual fits lead to tighter scaling relations. We have also checked that our results hold for all parameterizations of the DM halos of SPARC galaxies used by Li et al. (2020).

The main results of our analysis are all summarized in Figure 2. The H I mass as a function of M_{200} of the 150 galaxies of the sample displays a linear correlation between the two parameters, without any sign of a break at high mass. This

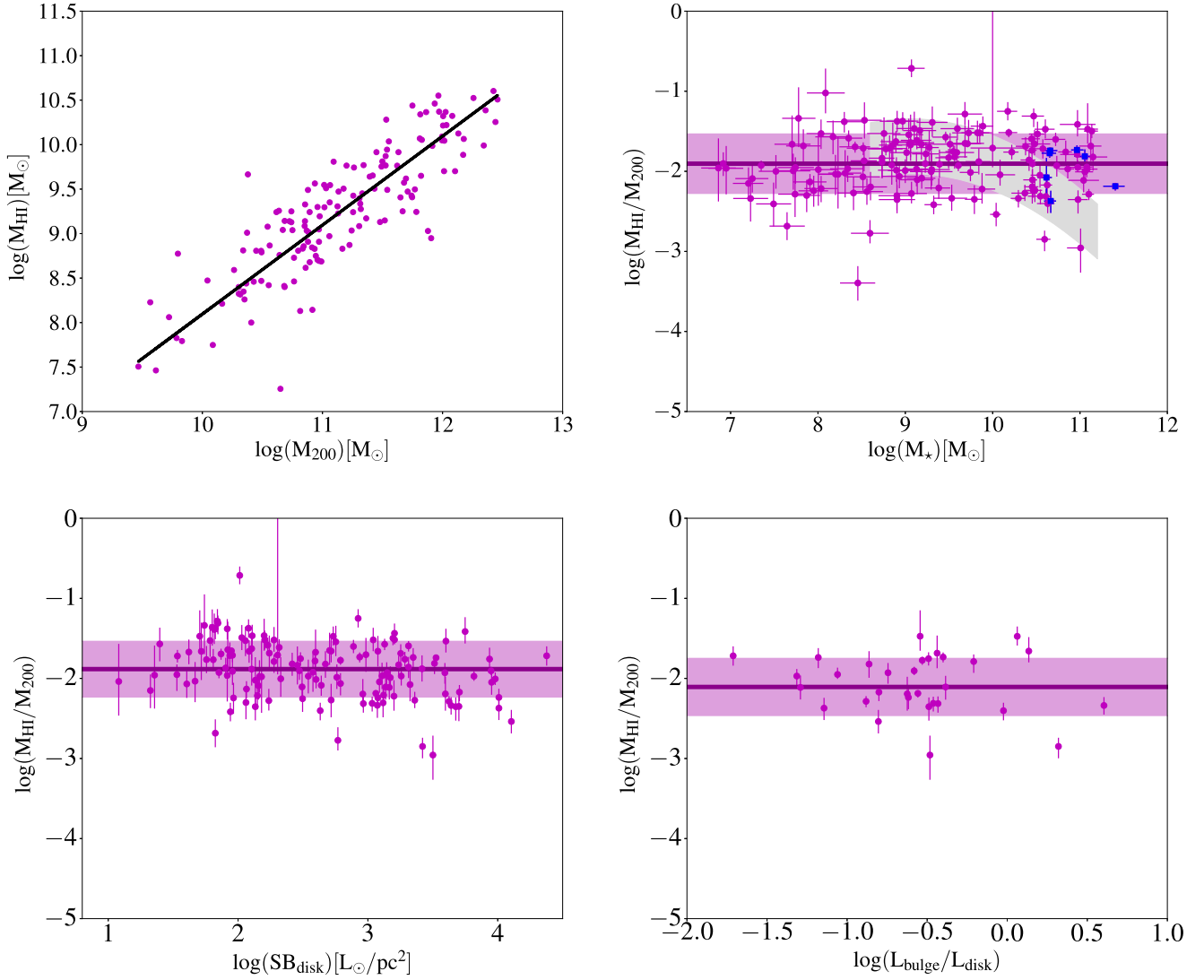


Figure 2. Top left: H I mass vs. halo mass for the 150 rotation curve fits with DZ profiles (magenta dots). The black line corresponds to the relation $M_{\text{HI}} = \log(\text{median}(M_{\text{HI}}/M_{200})) \times M_{200}$. Top right: H I-to-halo-mass ratio vs. stellar mass for the same sample (magenta dots with their associated error bars); the magenta line corresponds to the median value, and the band corresponds to the 1σ zone (scatter = 0.37 dex; intrinsic scatter = 0.31 dex). Blue squares depict galaxies hosting an AGN. The gray band indicates the 1σ band from isolated disks in SIMBA as a comparison. Bottom left: H I-to-halo-mass ratio for the DZ fits of the SPARC galaxies as a function of disk central surface brightness at $3.6 \mu\text{m}$. Bottom right: same as a function of bulge-to-disk-luminosity ratio for 31 galaxies with bulge.

implies that the H I mass is linearly increasing with halo mass for isolated disk galaxies in the local Universe. In other words, the H I-mass-to-halo-mass ratio of disk galaxies appears to be compatible with being constant. To check that this finding is independent of stellar mass, we display the ratio M_{HI}/M_{200} as a function of stellar mass, with the error bars as estimated from the DZ profile parameterization. The ratio is indeed compatible with a constant value of 1.25% (i.e., $\log(M_{\text{HI}}/M_{200}) = -1.903$) and an intrinsic scatter of 0.31 dex, namely a factor of 2, which is remarkable given that the sample spans 4 orders of magnitude in stellar mass. Note that this ratio does remain constant with stellar mass when using the NFW parameterization, too, albeit with a higher intrinsic scatter of 0.37 dex. Therefore, accounting for the actual diversity of rotation curve shapes (and DM profile cores and cusps) in our observational fits decreases the scatter of the ratio while keeping the ratio itself constant, which strengthens the robustness of the result. This is to be contrasted with the results from state-of-the-art simulations where the ratio decreases significantly at high masses. As a caveat, we note that the precise

selection function to get the exact same population in simulations is not known, but we checked that the simulated disk galaxies having the *highest* M_{HI}/M_{200} with $M_*/M_{\odot} > 10^{11}$ fall below the median of the observations (Figure A1).

To assess the robustness of our finding on this relatively small sample, we performed a Kolmogorov–Smirnov test on M_{HI}/M_{200} based on stellar mass using our sample of 150 galaxies. The test was run to compare the cumulative distributions of two data sets: galaxies with $10^8 \leq M_*/M_{\odot} < 10^{10}$ and galaxies with $M_* \geq 10^{10} M_{\odot}$. We found a statistic of 0.194 and a p value of 0.154; hence, the null hypothesis that the two samples are indeed drawn from the same distribution cannot be rejected. Although not statistically significant based on our sample size, we nevertheless note that when binning the data, a small downward trend seems to appear at the lowest mass end (Figure A1). Interestingly, we find that, at the high-mass end, massive disks hosting active galactic nuclei (AGNs) identified based on their X-ray emission (e.g., from XMM-Newton and Chandra) follow exactly the same relation as the other galaxies (Figure 2).

We also checked that the ratio remained constant over ~ 3 orders of magnitude in surface brightness in DZ fits (note that NFW fits did lead to a dependency here but associated to the fact that low surface brightness galaxies have a higher tendency to be actually cored) and that it did not depend on whether the galaxy hosts a bulge (which corresponds to 31 galaxies in total).

5. Conclusion

In this Letter, we report on the unexpected universality of the M_{HI}/M_{200} ratio for isolated disk galaxies with extended H I rotation curves in the local Universe. From our study, there appears to be no correlation between the halo mass, stellar mass, or surface brightness of disk galaxies and their M_{HI}/M_{200} ratio, which remains remarkably universal at a value of $\sim 1.25\%$, within a factor of 2 at 1σ . While it has been known for a long time that both stellar mass and total baryonic mass vary strongly across the disk galaxy population, it appears that this is not the case for H I in isolated disks. That the H I mass of an isolated disk galaxy is a direct tracer of its halo mass appears counterintuitive and could hint at interesting self-regulating mechanisms. Studying how this M_{HI}/M_{200} ratio varies when quenching takes place to transform star-forming galaxies into gas-poor red and dead ones would be an interesting follow-up to understand both the self-regulation mechanisms at play and the dominant quenching mechanisms.

It had already been shown that the SHMR of isolated disk galaxies appears to be a simple power law with no turnover at high masses, indicating that the fundamental parameters of disk galaxies may be single-slope monotonic functions of mass, with a small scatter, instead of being complicated non-monotonic functions (Posti et al. 2019). The present finding confirms this picture in a spectacular fashion: the M_{HI}/M_{200} ratio of disks does not even depend on mass.

A corollary of the single power-law SHMR for isolated disks is that massive disks are actually too DM dominated within modern state-of-the-art simulations of galaxy formation (Marasco et al. 2020). In other words, the simulated SHMR does not vary with disk fraction and Hubble type as it should from observations (Posti & Fall 2021), and AGN feedback does not seem to work as expected from simulations in observed disk galaxies, i.e., not expelling as many baryons from massive halos as expected, a problem known as the “failed feedback” problem. Interestingly, AGN-hosting galaxies follow exactly the same trend as other galaxies in our observed sample, supporting the “failed feedback” interpretation of this discrepancy.

The discrepancy between our findings and the simulations TNG50 and SIMBA, where the M_{HI}/M_{200} ratio decreases with mass for massive disks, is therefore yet another manifestation of the fact that simulated massive disks are too DM dominated indeed.

We note that alternative frameworks having the baryonic Tully–Fisher built-in as a fundamental relation (Milgrom 1983; Famaey & McGaugh 2012) do predict a monotonically rising SHMR and baryonic-to-halo mass relation (BHMR), but the universality of the H I HMR reported here does not follow naturally from there, as it results from a conspiracy between the BHMR (following from the baryonic Tully–Fisher relation) and

the scaling relation between the stellar and gas mass of galaxies (Oria et al. 2021), so as to yield a universal M_{HI}/M_{200} ratio.

In conclusion, this universal ratio points to isolated rotationally supported star-forming disk galaxies of all masses and surface densities being surprisingly self-similar, which hints at mass-independent self-regulation mechanisms that are yet to be fully understood.

Acknowledgments

The authors thank the anonymous referee for a thoughtful report that helped improve the manuscript. They thank Dylan Nelson for providing detailed information on the Illustris-TNG hydrodynamical simulations. The authors also thank Romeel Davé for making the hydrodynamical simulation Simba publicly available. They are grateful to Natasha Maddox for useful discussions. M.K. acknowledges funding from the Schlumberger Foundation Faculty for the Future program, and from the Observatoire Astronomique de Strasbourg (ObAS). M.K. acknowledges financial support from the Women by Science Programme of the Fundación Mujeres por África, from the Gobierno de Canarias, and from the Instituto de Astrofísica de Canarias (IAC). B.F., J.F., L.P. and R.I. acknowledge funding from the European Research Council (ERC) under the European Unions Horizon 2020 research and innovation program (grant agreement No. 834148) and from the Agence Nationale de la Recherche (ANR projects ANR-18-CE31-0006 and ANR-19-CE31-0017). D.E.-A. also acknowledges financial support from MICINN (Spain) through the program Juan de la Cierva. D.E.-A. acknowledges support from the Spanish Ministry of Science, Innovation, and Universities (MCIU), Agencia Estatal de Investigación (AEI), and the Fondo Europeo de Desarrollo Regional (EU-FEDER) under projects with references AYA2015-68217-P and PID2019-107010GB-100. C.R.A. acknowledges the project “Feeding and feedback in active galaxies”, with reference PID2019-106027GB-C42, funded by MICINN-AEI/10.13039/501100011033.

Appendix A

Stellar versus Gas Masses and Binned Data

To broadly compare the subpopulation of galaxies studied here with the general population and with the simulations, we show in Figure A1 the distribution of gas versus stellar mass of the TNG50 centrals, the SIMBA disks, and the observed galaxies analyzed here, together with isocontours from the general population of the blind extragalactic H I survey ALFALFA. One has, however, to keep in mind that all the observational results reported in this Letter pertain to regularly rotating extended H I disks. For instance, if observed earlier-type galaxies were included at the high-mass end, the observational data set would naturally also turn down to some degree at the high-mass end. Also, since the simulated data is binned in the rest of the paper, we display in Figure A1 our main result when the observed data is binned, showing a slight downward trend at the low-mass end. Finally, Figure A1 also displays the two simulated disk galaxies in both TNG50 and SIMBA having the highest M_{HI}/M_{200} with $M_*/M_\odot > 10^{11}$: since those still fall below the median of the observations, it confirms a tension independently of the above caveats.

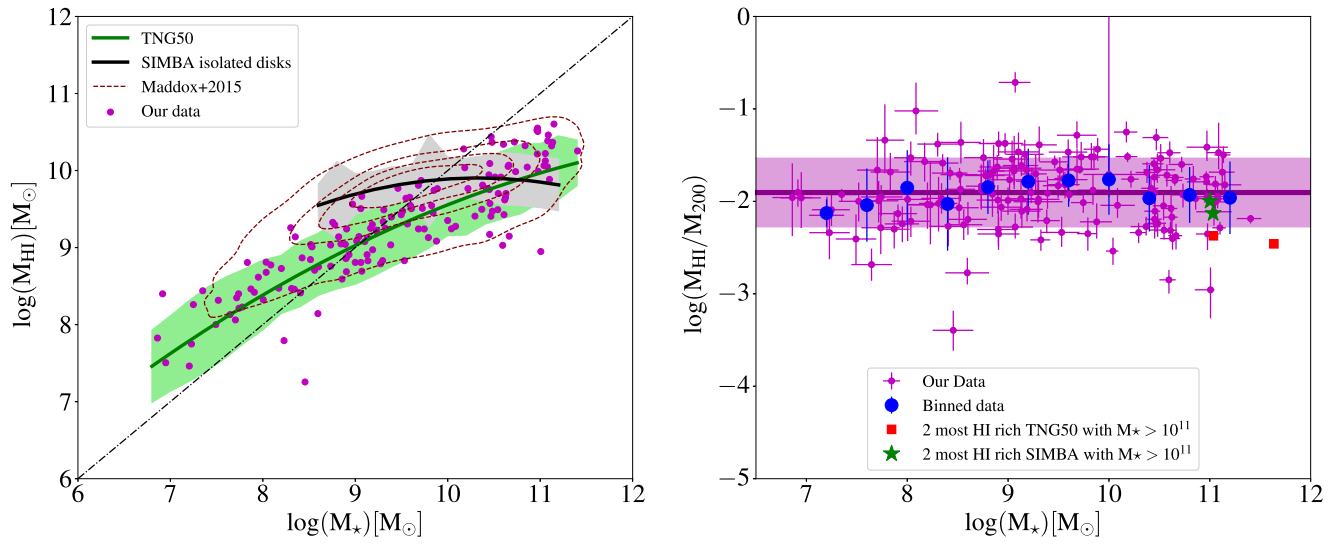


Figure A1. Left panel: H I mass as a function of stellar mass. The individual measurements for the 150 galaxies are presented as magenta dots. The contours correspond to the 9153 H I-selected ALFALFA galaxies from Maddox et al. (2015; see that paper for details). The green and gray lines (bands) represent the median (1σ scatter) of the binned data of central galaxies in Illustris-TNG50 and isolated disk galaxies in SIMBA, respectively. The diagonal dashed line marks the one-to-one relation of equal H I and stellar masses. Right panel: H I-to-Halo-mass ratio vs. stellar mass for the 150 galaxies with blue circles indicating the median and scatter in each bin. The two simulated disk galaxies in both Illustris-TNG50 and SIMBA having $M_{\star}/M_{\odot} > 10^{11}$ and the highest M_{HI}/M_{200} are represented as red squares and green stars, respectively.

Appendix B Rotation Curve Fits

We show in Figure B1 the model rotation curve fit (posterior distribution and rotation curve with its decomposition in different components) for the galaxy F568-1, as an example. The top panels show the results using the NFW parameterization, while the bottom panels depict those using the DZ parameterization. The fitted parameters for all 150 galaxies are listed in Table B1.

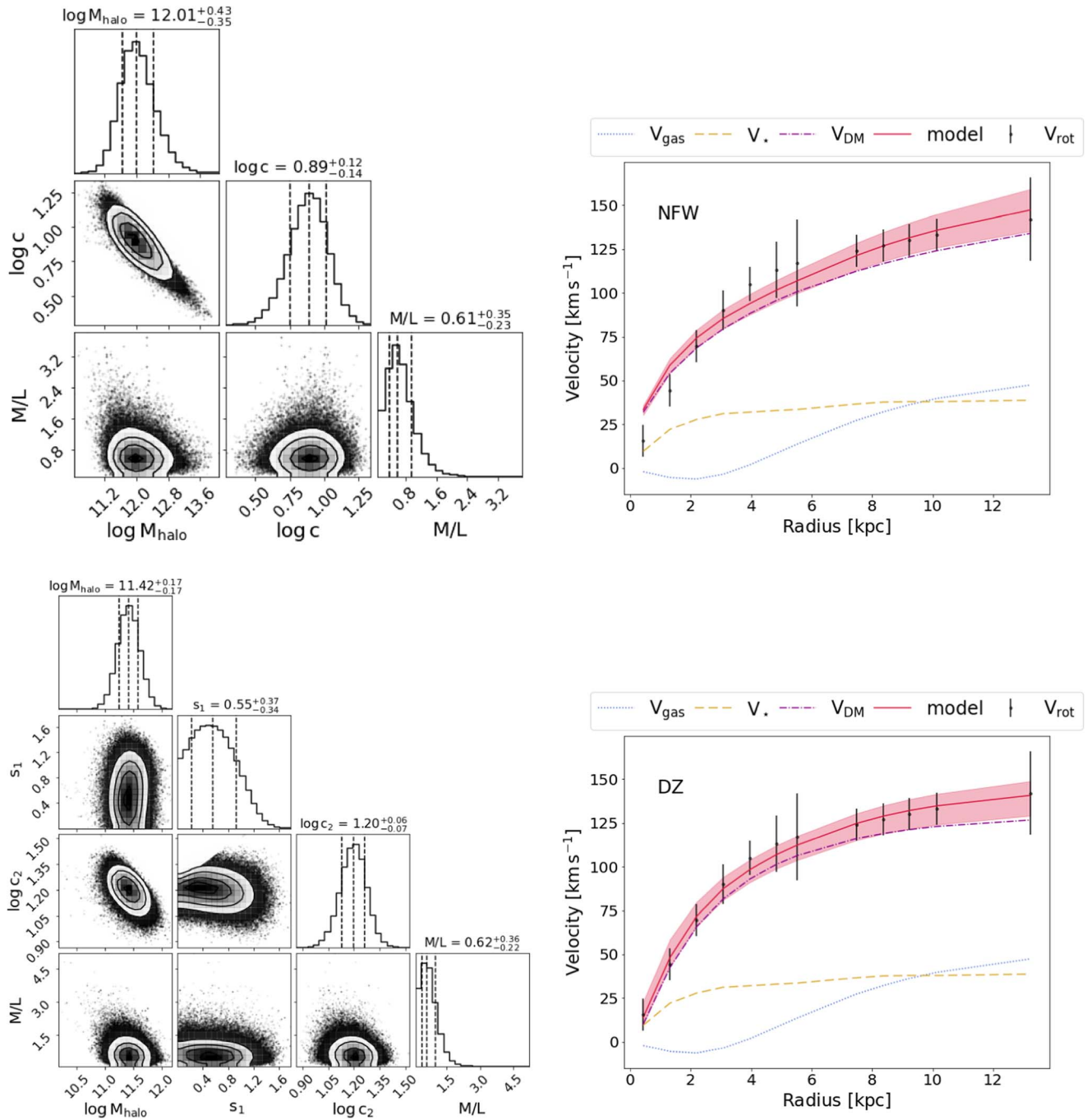


Figure B1. Galaxy F568-1. Top row: NFW; left panels: posterior distributions and mass model in right panel. Bottom row: DZ; left panels: posterior distributions and mass model in right panel.

Table B1
Fitted Parameters for All 150 Galaxies

Galaxy (1)	$M_{\star\text{NFW}}$ (2)	16th (3)	84th (4)	$M_{\star\text{TDZ}}$ (5)	16th (6)	84th (7)	M_{HI} (8)	M_{HNFw} (9)	16th (10)	84th (11)	M_{HDZ} (12)	16th (13)	84th (14)	χ^2_{NFW} (15)	χ^2_{TDZ} (16)
D564-8	7.19	7.01	7.36	7.20	7.02	7.37	7.46	9.36	9.14	9.60	9.61	9.41	9.83	5.26	0.63
D631-7	7.84	7.67	7.99	7.87	7.70	8.02	8.46	10.84	10.60	11.10	10.76	10.56	10.97	9.86	2.22
DDO064	7.97	7.77	8.18	8.00	7.79	8.22	8.32	10.17	9.67	10.71	10.30	9.86	10.75	1.14	0.46
DDO154	7.19	7.04	7.33	7.35	7.19	7.50	8.43	10.77	10.66	10.89	10.36	10.30	10.43	11.52	2.51
DDO161	8.31	8.15	8.47	8.35	8.18	8.50	9.13	10.83	10.71	10.97	10.72	10.62	10.83	3.76	2.21
DDO168	7.91	7.73	8.07	7.95	7.77	8.11	8.61	11.08	10.80	11.41	10.85	10.67	11.05	14.91	4.94
DDO170	8.41	8.23	8.58	8.42	8.24	8.59	8.86	10.64	10.56	10.73	10.56	10.49	10.63	3.07	2.36
ESO079-G014	10.43	10.28	10.56	10.36	10.21	10.51	9.49	12.31	12.08	12.58	11.76	11.66	11.86	4.40	1.70
ESO116-G012	9.32	9.18	9.44	9.38	9.22	9.51	9.03	11.72	11.52	11.99	11.24	11.12	11.37	2.58	1.18
ESO444-G084	7.60	7.41	7.79	7.64	7.44	7.84	8.13	11.18	10.92	11.53	10.81	10.64	10.98	0.89	0.17
ESO563-G021	11.38	11.32	11.43	11.08	10.94	11.20	10.38	12.88	12.69	13.11	12.35	12.29	12.41	18.65	7.71
F563-1	9.05	8.86	9.25	9.05	8.86	9.25	9.50	11.41	11.19	11.66	11.17	11.01	11.32	1.19	0.52
F563-V2	9.28	9.08	9.49	9.30	9.09	9.51	9.33	11.91	11.48	12.41	11.31	11.10	11.51	1.36	0.43
F565-V2	8.51	8.32	8.71	8.51	8.32	8.70	8.84	11.09	10.85	11.38	10.91	10.75	11.08	1.39	0.44
F568-1	9.58	9.38	9.77	9.58	9.38	9.78	9.65	12.01	11.65	12.45	11.41	11.24	11.58	0.99	0.14
F568-V1	9.40	9.20	9.61	9.39	9.18	9.59	9.39	11.67	11.36	12.07	11.30	11.12	11.47	0.53	0.18
F571-8	9.22	9.10	9.33	9.32	9.22	9.41	9.25	12.40	12.14	12.72	11.66	11.55	11.78	5.34	1.10
F571-V1	9.01	8.82	9.20	9.01	8.82	9.20	9.08	10.97	10.79	11.18	10.85	10.71	10.99	0.91	0.49
F574-1	9.59	9.40	9.78	9.59	9.40	9.78	9.54	11.29	11.08	11.52	11.01	10.87	11.15	1.83	0.17
F579-V1	9.97	9.75	10.20	9.99	9.74	10.38	9.35	11.25	10.82	11.59	11.06	8.52	11.30	1.13	0.37
F583-1	8.75	8.55	8.94	8.75	8.56	8.94	9.32	11.00	10.73	11.30	10.85	10.65	11.05	2.41	0.46
F583-4	9.03	8.82	9.26	9.06	8.84	9.33	8.80	10.56	10.21	10.87	10.44	10.09	10.67	0.61	0.37
IC2574	8.59	8.42	8.74	8.52	8.37	8.67	9.01	11.31	11.13	11.51	10.88	10.75	11.01	43.56	4.96
IC4202	10.61	10.48	10.73	10.45	10.33	10.56	10.09	12.38	12.28	12.50	11.99	11.94	12.04	26.90	7.30
KK98-251	7.88	7.60	8.41	7.70	7.50	7.91	8.06	9.09	4.64	9.55	9.72	9.36	10.08	5.52	1.20
NGC0024	9.62	9.46	9.74	9.53	9.32	9.70	8.83	11.33	11.12	11.59	11.16	10.99	11.32	0.89	0.84
NGC0055	9.20	9.04	9.35	9.23	9.07	9.38	9.19	11.18	10.98	11.42	10.97	10.83	11.12	4.66	1.39
NGC0100	9.16	8.99	9.31	9.18	9.01	9.33	9.29	11.24	10.96	11.57	10.95	10.76	11.15	1.76	0.18
NGC0247	9.62	9.44	9.79	9.68	9.47	9.90	9.24	11.32	11.09	11.55	10.89	10.67	11.07	2.12	2.09
NGC0289	10.61	10.50	10.70	10.47	10.33	10.58	10.43	11.84	11.75	11.94	11.74	11.65	11.88	1.94	2.45
NGC0300	9.16	8.99	9.31	9.18	9.01	9.34	8.97	11.36	11.17	11.58	11.05	10.93	11.18	0.81	0.52
NGC0801	11.23	11.20	11.26	11.13	11.04	11.20	10.36	11.98	11.89	12.09	11.86	11.77	11.95	7.45	10.63
NGC0891	10.69	10.64	10.73	10.62	10.54	10.68	9.65	12.25	12.06	12.51	11.82	11.73	11.93	5.67	3.54
NGC1003	9.49	9.35	9.61	9.46	9.31	9.59	9.76	11.48	11.39	11.58	11.34	11.27	11.41	3.18	4.83
NGC1090	10.55	10.46	10.62	10.44	10.33	10.54	9.94	11.73	11.64	11.83	11.53	11.47	11.60	2.51	1.31
NGC1705	8.77	8.58	8.92	8.59	8.37	8.81	8.14	10.99	10.70	11.40	10.91	10.75	11.04	0.94	0.14
NGC2366	7.96	7.80	8.12	8.03	7.86	8.18	8.81	10.50	10.28	10.76	10.33	10.16	10.53	4.83	1.05
NGC2403	9.67	9.58	9.74	9.60	9.48	9.74	9.50	11.44	11.37	11.52	11.43	11.36	11.50	9.92	9.48
NGC2683	10.73	10.67	10.77	10.66	10.58	10.72	9.14	11.65	11.49	11.82	11.51	11.39	11.66	1.34	0.99
NGC2841	11.24	11.20	11.28	10.97	10.86	11.08	9.99	12.55	12.44	12.67	12.34	12.22	12.51	1.82	2.32
NGC2903	10.51	10.46	10.55	10.46	10.40	10.52	9.40	11.82	11.74	11.92	11.64	11.57	11.73	8.95	6.00
NGC2915	8.56	8.37	8.74	8.56	8.37	8.74	8.70	11.14	10.91	11.42	10.95	10.79	11.12	1.24	0.97
NGC2955	11.21	11.18	11.24	11.08	10.97	11.20	10.46	12.13	11.80	12.45	11.93	11.61	12.11	4.80	2.76
NGC2998	10.96	10.87	11.03	10.72	10.59	10.83	10.37	12.02	11.93	12.13	11.97	11.88	12.05	2.74	1.10
NGC3109	8.00	7.81	8.19	8.03	7.84	8.22	8.67	11.37	11.11	11.65	10.89	10.73	11.06	13.24	1.07
NGC3198	10.30	10.21	10.36	10.18	10.06	10.28	10.03	11.68	11.62	11.75	11.55	11.50	11.61	1.48	0.82
NGC3521	10.64	10.59	10.68	10.61	10.51	10.67	9.61	12.31	11.88	12.79	11.69	11.45	11.90	0.28	0.69
NGC3726	10.44	10.35	10.52	10.37	10.26	10.47	9.81	11.76	11.58	11.95	11.49	11.38	11.61	2.95	3.60
NGC3741	7.16	6.97	7.34	7.24	7.05	7.43	8.26	10.46	10.26	10.70	10.35	10.18	10.52	1.58	1.04
NGC3769	9.90	9.78	10.00	9.85	9.72	9.96	9.74	11.42	11.27	11.58	11.26	11.14	11.38	0.91	0.69
NGC3893	10.47	10.40	10.52	10.41	10.31	10.49	9.76	12.06	11.82	12.37	11.62	11.49	11.75	1.40	0.41
NGC3917	10.21	10.06	10.46	10.08	9.91	10.25	9.27	11.59	10.40	11.91	11.31	11.13	11.45	4.11	0.89
NGC3972	9.84	9.68	9.99	9.87	9.71	10.02	9.08	11.95	11.56	12.37	11.30	11.10	11.48	1.43	0.76
NGC3992	11.25	11.19	11.30	11.05	10.93	11.15	10.22	12.16	12.05	12.29	12.03	11.94	12.16	0.85	0.61
NGC4010	9.83	9.68	9.97	9.84	9.69	9.97	9.45	11.79	11.48	12.14	11.33	11.16	11.49	2.97	2.37
NGC4013	10.60	10.54	10.65	10.48	10.38	10.56	9.47	11.96	11.81	12.14	11.70	11.60	11.85	1.31	2.34
NGC4085	9.77	9.65	9.88	9.79	9.68	9.88	9.13	12.30	11.82	12.84	11.47	11.30	11.66	5.05	2.39
NGC4088	10.55	10.47	10.62	10.51	10.41	10.59	9.91	11.73	11.50	11.98	11.44	11.29	11.59	0.66	0.97
NGC4100	10.62	10.55	10.68	10.54	10.43	10.62	9.49	11.73	11.54	11.94	11.53	11.39	11.69	1.31	0.93
NGC4138	10.50	10.43	10.56	10.45	10.36	10.52	9.17	11.52	11.19	11.84	11.36	11.15	11.57	1.71	1.76
NGC4157	10.64	10.56	10.71	10.57	10.47	10.66	9.91	11.96	11.76	12.18	11.63	11.51	11.75	0.56	0.93
NGC4183	9.86	9.68	10.01	9.82	9.64	9.99	9.54	11.18	11.00	11.36	11.06	10.91	11.20	0.19	0.17
NGC4214	8.95	8.79	9.08	8.90	8.69	9.08	8.68	11.31	10.92	11.81	10.99	10.79	11.17	0.91	0.48

Table B1
(Continued)







Galaxy (1)	M_{NFW} (2)	16th (3)	84th (4)	M_{DZ} (5)	16th (6)	84th (7)	M_{HI} (8)	M_{NFW} (9)	16th (10)	84th (11)	M_{DZ} (12)	16th (13)	84th (14)	χ^2_{NFW} (15)	χ^2_{DZ} (16)
NGC4217	10.33	10.26	10.40	10.29	10.20	10.36	9.40	12.41	12.13	12.77	11.74	11.64	11.86	5.27	2.52
NGC4559	9.92	9.79	10.03	9.88	9.74	10.00	9.76	11.39	11.23	11.58	11.20	11.07	11.32	0.39	0.45
NGC5033	10.74	10.66	10.80	10.65	10.56	10.72	10.05	11.94	11.88	11.99	11.82	11.78	11.88	5.21	2.51
NGC5055	10.70	10.66	10.72	10.66	10.56	10.74	10.06	11.83	11.81	11.86	11.81	11.77	11.84	3.12	2.92
NGC5371	11.22	11.16	11.27	11.07	11.00	11.14	10.04	11.61	11.49	11.72	11.99	11.84	12.12	9.65	1.55
NGC5585	8.92	8.80	9.03	9.22	9.16	9.27	9.22	11.42	11.27	11.61	11.13	11.02	11.24	6.25	5.22
NGC5907	11.07	11.00	11.11	10.83	10.75	10.90	10.32	12.02	11.94	12.12	12.08	11.93	12.23	6.39	3.13
NGC5985	11.43	11.32	11.49	11.04	10.86	11.21	10.06	11.99	11.72	12.18	12.17	12.02	12.32	8.09	2.44
NGC6015	10.39	10.33	10.43	10.21	10.12	10.29	9.76	11.67	11.54	11.83	11.52	11.43	11.61	8.45	7.44
NGC6195	11.29	11.26	11.31	11.12	10.99	11.24	10.32	12.13	11.94	12.34	12.00	11.78	12.19	3.47	3.43
NGC6503	9.78	9.71	9.85	9.74	9.62	9.83	9.24	11.31	11.24	11.38	11.25	11.17	11.36	1.86	1.56
NGC6674	11.30	11.26	11.34	10.97	10.88	11.04	10.50	12.41	12.32	12.51	12.45	12.37	12.51	6.37	7.61
NGC6946	10.48	10.43	10.52	10.45	10.37	10.50	9.75	11.84	11.65	12.09	11.49	11.37	11.62	1.99	1.58
NGC7331	10.97	10.93	11.00	10.86	10.75	10.93	10.04	12.40	12.24	12.58	12.01	11.92	12.13	0.80	2.54
NGC7814	10.68	10.63	10.73	10.59	10.50	10.66	9.02	12.30	12.10	12.56	11.87	11.77	12.02	1.79	0.55
UGC00128	9.82	9.63	9.98	9.71	9.54	9.86	9.87	11.56	11.53	11.59	11.52	11.48	11.57	3.28	3.85
UGC00191	9.12	8.96	9.26	9.13	8.94	9.29	9.12	10.94	10.86	11.04	10.74	10.63	10.85	3.85	2.69
UGC00731	8.29	8.09	8.49	8.30	8.10	8.50	9.25	10.77	10.64	10.92	10.63	10.51	10.77	0.38	0.11
UGC01230	9.70	9.50	9.90	9.68	9.48	9.87	9.80	11.20	11.01	11.38	11.09	10.94	11.23	1.20	0.38
UGC01281	8.31	8.11	8.52	8.31	8.11	8.49	8.46	10.46	10.10	10.85	10.49	10.20	10.79	2.84	0.29
UGC02259	9.18	8.97	9.38	9.07	8.87	9.24	8.69	10.81	10.71	10.92	10.97	10.82	11.09	1.42	1.01
UGC02487	11.71	11.66	11.75	11.40	11.26	11.51	10.25	12.59	12.53	12.67	12.44	12.40	12.49	5.37	5.04
UGC02885	11.41	11.35	11.46	11.14	10.98	11.31	10.60	12.60	12.47	12.76	12.42	12.26	12.59	1.56	3.69
UGC02916	10.71	10.69	10.74	10.47	10.34	10.65	10.36	12.17	12.00	12.37	12.02	11.85	12.16	11.32	6.60
UGC02953	11.19	11.16	11.21	11.10	11.02	11.16	9.88	12.32	12.26	12.40	12.17	12.10	12.24	7.33	6.15
UGC03205	10.93	10.88	10.96	10.73	10.62	10.82	9.98	12.10	11.97	12.27	11.91	11.79	12.05	3.53	3.04
UGC03546	10.68	10.62	10.73	10.60	10.53	10.67	9.42	11.98	11.86	12.14	11.74	11.65	11.85	2.08	0.82
UGC03580	9.49	9.41	9.55	9.54	9.45	9.61	9.64	11.58	11.48	11.69	11.39	11.31	11.47	3.89	4.85
UGC04278	8.81	8.62	8.98	8.84	8.66	9.01	9.04	11.23	10.88	11.63	10.97	10.73	11.21	3.11	1.51
UGC04325	9.38	9.14	9.59	9.29	9.05	9.54	8.83	10.86	10.56	11.09	10.83	10.56	11.06	3.33	3.76
UGC04483	6.85	6.66	7.03	6.94	6.74	7.14	7.50	9.26	8.97	9.62	9.46	9.18	9.79	0.92	0.60
UGC04499	8.86	8.69	9.01	8.89	8.71	9.04	9.04	10.85	10.67	11.06	10.66	10.53	10.81	1.48	0.34
UGC05005	9.30	9.12	9.47	9.30	9.12	9.48	9.49	11.03	10.78	11.26	10.87	10.68	11.06	1.99	1.88
UGC05253	10.96	10.94	10.97	10.96	10.77	10.99	10.21	12.20	12.11	12.30	12.00	11.91	12.14	3.41	2.57
UGC05414	8.65	8.48	8.81	8.73	8.57	8.87	8.75	10.92	10.63	11.26	10.64	10.45	10.84	3.27	0.40
UGC05716	8.47	8.30	8.63	8.51	8.33	8.69	9.03	10.83	10.77	10.89	10.75	10.67	10.83	2.02	2.46
UGC05721	8.68	8.50	8.83	8.60	8.39	8.79	8.75	11.01	10.78	11.33	10.94	10.75	11.11	2.20	1.72
UGC05764	7.75	7.54	7.96	7.74	7.53	7.95	8.21	10.31	10.22	10.41	10.16	10.03	10.36	7.85	5.02
UGC05829	8.52	8.32	8.72	8.53	8.33	8.73	9.01	10.40	10.13	10.71	10.37	10.14	10.60	1.10	0.33
UGC05918	8.15	7.95	8.36	8.17	7.96	8.37	8.47	10.03	9.79	10.31	10.04	9.83	10.25	0.39	0.04
UGC05986	9.48	9.35	9.59	9.49	9.34	9.61	9.42	11.92	11.67	12.26	11.25	11.14	11.39	6.06	0.87
UGC06399	9.12	8.93	9.31	9.13	8.94	9.32	8.82	11.20	10.92	11.52	10.93	10.75	11.11	1.03	0.06
UGC06446	8.83	8.63	9.02	8.82	8.61	9.02	9.14	10.98	10.77	11.22	10.85	10.68	11.01	0.38	0.22
UGC06614	10.67	10.57	10.76	10.60	10.47	10.70	10.34	12.19	12.01	12.38	11.81	11.69	11.92	0.59	2.86
UGC06667	8.93	8.73	9.13	8.93	8.73	9.13	8.90	11.37	11.15	11.65	10.97	10.84	11.11	1.63	0.28
UGC06786	10.68	10.62	10.72	10.54	10.40	10.64	9.70	12.27	12.16	12.41	12.01	11.93	12.11	1.92	0.99
UGC06787	10.72	10.67	10.76	10.63	10.50	10.70	9.70	12.21	12.13	12.29	12.10	12.00	12.22	28.04	26.56
UGC06818	8.74	8.58	8.89	8.73	8.58	8.87	9.03	10.86	10.55	11.20	10.86	10.63	11.10	6.06	3.47
UGC06917	9.54	9.37	9.69	9.56	9.39	9.71	9.30	11.45	11.23	11.72	11.12	10.98	11.27	0.94	0.28
UGC06923	9.10	8.94	9.25	9.12	8.97	9.25	8.90	11.11	10.77	11.52	10.87	10.67	11.09	1.47	0.94
UGC06930	9.74	9.55	9.91	9.72	9.53	9.90	9.51	11.17	10.97	11.39	11.02	10.86	11.17	0.33	0.19
UGC06973	10.04	10.00	10.08	10.04	9.97	10.09	9.24	12.95	12.46	13.52	11.78	11.63	11.93	1.37	1.12
UGC06983	9.54	9.36	9.71	9.51	9.32	9.68	9.47	11.34	11.15	11.56	11.13	10.99	11.27	0.72	0.50
UGC07125	9.06	8.90	9.21	9.07	8.90	9.22	9.66	10.40	10.28	10.53	10.37	10.26	10.48	1.83	0.91
UGC07151	9.21	9.06	9.33	9.27	9.12	9.38	8.79	10.77	10.48	11.08	10.49	10.28	10.70	2.76	1.08
UGC07261	9.05	8.87	9.20	9.04	8.85	9.20	9.14	10.77	10.51	11.07	10.68	10.48	10.86	0.20	0.08
UGC07399	8.98	8.78	9.16	8.90	8.69	9.11	8.87	11.49	11.24	11.84	11.22	11.04	11.39	1.75	1.05
UGC07524	9.13	8.93	9.31	9.16	8.97	9.35	9.25	10.93	10.73	11.16	10.74	10.58	10.89	1.32	0.36
UGC07559	7.83	7.61	8.17	7.77	7.59	7.97	8.22	9.13	6.75	9.56	9.56	9.17	9.92	1.99	0.30
UGC07603	8.30	8.13	8.46	8.40	8.21	8.56	8.41	11.00	10.71	11.38	10.68	10.47	10.89	1.71	0.79
UGC07608	8.19	7.99	8.38	8.20	8.00	8.39	8.72	10.94	10.59	11.36	10.76	10.52	11.02	1.15	0.06
UGC07690	8.84	8.71	8.95	8.85	8.69	8.96	8.59	10.22	9.90	10.54	10.26	9.98	10.49	0.54	0.75
UGC08286	9.07	8.87	9.23	8.99	8.80	9.18	8.80	10.93	10.80	11.09	10.79	10.65	10.95	2.39	1.77

Table B1
(Continued)

Galaxy (1)	M_{NFW} (2)	16th (3)	84th (4)	M_{DZ} (5)	16th (6)	84th (7)	M_{HI} (8)	M_{NFW} (9)	16th (10)	84th (11)	M_{DZ} (12)	16th (13)	84th (14)	χ^2_{NFW} (15)	χ^2_{DZ} (16)
UGC08490	8.95	8.77	9.10	8.89	8.68	9.08	8.85	10.84	10.70	11.02	10.84	10.68	10.98	0.53	0.37
UGC08550	8.29	8.11	8.45	8.34	8.13	8.51	8.45	10.50	10.34	10.70	10.42	10.26	10.59	0.74	0.58
UGC08699	10.49	10.46	10.52	10.45	10.35	10.51	9.57	12.00	11.81	12.24	11.67	11.54	11.83	1.27	1.12
UGC09037	10.19	10.08	10.30	10.17	10.05	10.28	10.28	11.88	11.69	12.10	11.53	11.41	11.64	2.44	1.92
UGC09133	11.17	11.14	11.19	10.96	10.89	11.04	10.52	12.22	12.19	12.26	12.25	12.19	12.32	8.92	7.85
UGC10310	9.07	8.87	9.27	9.10	8.89	9.30	9.07	10.65	10.38	10.93	10.54	10.33	10.73	0.63	0.37
UGC11455	11.22	11.15	11.27	11.05	10.94	11.15	10.12	12.60	12.42	12.80	12.13	12.05	12.20	5.60	1.93
UGC11820	8.69	8.51	8.85	8.77	8.57	8.96	9.29	11.11	11.02	11.23	11.01	10.93	11.09	2.15	5.31
UGC11914	11.02	10.99	11.04	11.00	10.85	11.04	8.94	13.02	12.50	13.59	11.90	11.66	12.21	2.54	2.68
UGC12506	11.12	10.95	11.27	10.97	10.76	11.17	10.55	12.16	11.91	12.37	11.96	11.78	12.11	0.97	0.21
UGC12632	8.90	8.70	9.09	8.90	8.70	9.10	9.24	10.71	10.55	10.88	10.61	10.48	10.75	0.40	0.09
UGC12732	8.96	8.77	9.14	8.97	8.78	9.15	9.56	11.09	10.96	11.25	10.93	10.82	11.05	0.36	0.67
UGCA281	8.07	7.88	8.27	8.22	8.01	8.40	7.79	9.78	9.23	10.32	9.83	9.36	10.25	0.92	0.35
UGCA442	7.87	7.69	8.06	7.90	7.71	8.09	8.42	10.86	10.72	11.03	10.55	10.45	10.66	3.27	1.43
UGCA444	6.85	6.65	7.06	6.86	6.66	7.06	7.82	9.57	9.18	10.01	9.78	9.41	10.20	0.57	0.16
ddo101	8.43	8.23	8.62	8.45	8.25	8.65	7.25	10.91	10.60	11.30	10.65	10.43	10.87	0.43	0.20
ddo133	7.48	7.28	7.67	7.49	7.29	7.69	8.00	10.56	10.19	11.00	10.40	10.14	10.68	0.76	0.12
ddo154	6.90	6.70	7.09	6.91	6.71	7.11	8.40	10.48	10.31	10.69	10.30	10.16	10.45	2.29	0.88
ddo168	7.72	7.53	7.90	7.73	7.54	7.92	8.40	10.70	10.36	11.09	10.68	10.41	10.97	3.80	0.79
ddo50	8.06	7.85	8.27	8.08	7.87	8.30	8.77	9.72	9.41	10.00	9.79	9.49	10.05	1.28	1.28
ddo52	7.70	7.51	7.89	7.71	7.51	7.91	8.34	10.38	10.11	10.70	10.34	10.12	10.57	1.42	0.17
ddo87	7.50	7.30	7.70	7.51	7.32	7.71	8.31	10.39	10.14	10.69	10.31	10.11	10.53	1.17	0.23
ngc2366	7.83	7.63	8.03	7.83	7.63	8.03	8.80	10.52	10.27	10.82	10.48	10.28	10.71	4.33	1.15
wlm	7.20	7.01	7.39	7.22	7.02	7.43	7.74	10.18	9.86	10.54	10.08	9.82	10.37	2.94	0.84

Note. Properties of the sample of 150 galaxies studied in this work: (1) name of the galaxy; (2)–(4) stellar mass in M_{\odot} from NFW fits with their 16th–84th percentiles; (5)–(7) stellar mass in M_{\odot} from DZ fits with their 16th–84th percentiles; (8) total H I mass in M_{\odot} from Iorio et al. (2017); (9)–(11) DM halo mass M_{200} in M_{\odot} from NFW fits with their 16th–84th percentiles; (12)–(14) DM halo mass M_{200} in M_{\odot} from DZ fits with their 16th–84th percentiles and (15)–(16) reduced χ^2 from NFW and DZ fits, respectively.

ORCID iDs

Marie Korsaga  <https://orcid.org/0000-0002-5882-610X>
 Benoit Famaey  <https://orcid.org/0000-0003-3180-9825>
 Jonathan Freundlich  <https://orcid.org/0000-0002-5245-7796>
 Lorenzo Posti  <https://orcid.org/0000-0001-9072-5213>
 Rodrigo Ibata  <https://orcid.org/0000-0002-3292-9709>
 Katarina Kraljic  <https://orcid.org/0000-0001-6180-0245>
 C. Ramos Almeida  <https://orcid.org/0000-0001-8353-649X>

References

- Behroozi, P. S., Conroy, C., & Wechsler, R. H. 2010, *ApJ*, **717**, 379
 Calette, A. R., Rodríguez-Puebla, A., Avila-Reese, V., & Lagos, V. 2021, *MNRAS*, **506**, 1507
 Chauhan, G., Lagos, C. d. P., Stevens, A. R., et al. 2021, *MNRAS*, **506**, 4893
 Davé, R., Anglés-Alcázar, D., Narayanan, D., et al. 2019, *MNRAS*, **486**, 2827
 Dekel, A., Ishai, G., Dutton, A. A., & Maccio, A. V. 2017, *MNRAS*, **468**, 1005
 Diemer, B., Stevens, A. R. H., Forbes, J. C., et al. 2018, *ApJS*, **238**, 33
 Dutta, S., Khandai, N., & Rana, S. 2022, *MNRAS*, **511**, 2585
 Dutton, A. A., & Macciò, A. V. 2014, *MNRAS*, **441**, 3359
 Famaey, B., & McGaugh, S. S. 2012, *LRR*, **15**, 10
 Foreman-Mackey, D., Hogg, D. W., Lang, D., & Goodman, J. 2013, *PASP*, **125**, 306
 Freundlich, J., Dekel, A., Jiang, F., et al. 2020, *MNRAS*, **491**, 4523
 Guo, H., Jones, M. G., Haynes, M. P., & Fu, J. 2020, *ApJ*, **894**, 92
 Guo, H., Li, C., Zheng, Z., et al. 2017, *ApJ*, **846**, 61
 Haardt, F., & Madau, P. 2012, *ApJ*, **746**, 125
 Hopkins, P. F. 2015, *MNRAS*, **450**, 53
 Hunter, D. A., Ficut-Vicas, D., Ashley, T., et al. 2012, *AJ*, **144**, 134
 Iorio, G., Fraternali, F., Nipoti, C., et al. 2017, *MNRAS*, **466**, 4159
 Krumholz, M. R., & Gnedin, N. Y. 2011, *ApJ*, **729**, 36
 Lelli, F. 2022, *NatAs*, **6**, 35
 Lelli, F., McGaugh, S. S., & Schombert, J. M. 2016, *AJ*, **152**, 157
 Lelli, F., McGaugh, S. S., Schombert, J. M., Desmond, H., & Katz, H. 2019, *MNRAS*, **484**, 3267
 Li, P., Lelli, F., McGaugh, S., & Schombert, J. 2020, *ApJS*, **247**, 31
 Maddox, N., Hess, K. M., Obreschkow, D., Jarvis, M. J., & Blyth, S. L. 2015, *MNRAS*, **447**, 1610
 Marasco, A., Posti, L., Oman, K., et al. 2020, *A&A*, **640**, A70
 McGaugh, S. S., & Schombert, J. M. 2014, *AJ*, **148**, 77
 McGaugh, S. S., Schombert, J. M., Bothun, G. D., & de Blok, W. J. G. 2000, *ApJ*, **533**, L99
 Meidt, S. E., Schinnerer, E., Van De Ven, G., et al. 2014, *ApJ*, **788**, 144
 Milgrom, M. 1983, *ApJ*, **270**, 365
 Moster, B. P., Naab, T., & White, S. D. M. 2013, *MNRAS*, **428**, 3121
 Moster, B. P., Somerville, R. S., Maulbetsch, C., et al. 2010, *ApJ*, **710**, 903
 Navarro, J. F., Frenk, C. S., & White, S. D. M. 1996, *ApJ*, **462**, 563
 Nelson, D., Pillepich, A., Springel, V., et al. 2018, *MNRAS*, **475**, 624
 Nelson, D., Pillepich, A., Springel, V., et al. 2019, *MNRAS*, **490**, 3234
 Obuljen, A., Alonso, D., Villaescusa-Navarro, F., Yoon, I., & Jones, M. 2019, *MNRAS*, **486**, 5124
 Oh, S.-H., Hunter, D. A., Brinks, E., et al. 2015, *AJ*, **149**, 180
 Oria, P. A., Famaey, B., Thomas, G. F., et al. 2021, *ApJ*, **923**, 68
 Padmanabhan, H., & Kulkarni, G. 2017, *MNRAS*, **470**, 340
 Padmanabhan, H., & Refregier, A. 2017, *MNRAS*, **464**, 4008
 Pillepich, A., Nelson, D., Hernquist, L., et al. 2018, *MNRAS*, **475**, 648
 Pillepich, A., Nelson, D., Springel, V., et al. 2019, *MNRAS*, **490**, 3196
 Poppinga, G., Behroozi, P. S., & Peebles, M. S. 2015, *MNRAS*, **449**, 477
 Posti, L., & Fall, S. M. 2021, *A&A*, **649**, 119
 Posti, L., Marasco, A., Fraternali, F., & Famaey, B. 2019, *A&A*, **629**, A59
 Rahmati, A., Pawlik, A. H., Raičević, M., & Schaye, J. 2013, *MNRAS*, **430**, 2427
 Read, J. I., Iorio, G., Agertz, O., & Fraternali, F. 2017, *MNRAS*, **467**, 2019
 Schaye, J., Crain, R. A., Bower, R. G., et al. 2015, *MNRAS*, **446**, 521
 Schombert, J., & McGaugh, S. 2014, *PASA*, **31**, e036
 Schombert, J., McGaugh, S., & Lelli, F. 2019, *MNRAS*, **483**, 1496
 Schombert, J., McGaugh, S., & Lelli, F. 2022, *AJ*, **163**, 154
 Springel, V. 2005, *MNRAS*, **364**, 1105
 Tacchella, S., Diemer, B., Hernquist, L., et al. 2019, *MNRAS*, **487**, 5416
 Zhao, H. 1996, *MNRAS*, **278**, 488